Climate Dynamics
https://doi.org/10.1007/s00382-022-06525-5

Impact of the leading atmospheric wave train over Eurasia on the climate variability over the Tibetan Plateau during early spring

Yaoxian Yang[1,2] · Yimin Liu[3,4] · Zeyong Hu[1,2] · Haipeng Yu[1,2] · Jinxiao Li[3] · Yongkun Xie[5] · Qian Yang[6]

Received: 4 April 2022 / Accepted: 24 September 2022

Abstract
The great potentials of unique spatiotemporal characteristics of springtime precipitation and surface air temperature over the Tibetan Plateau (TP) act as a new source of predictability to improve the climate prediction in the TP and neighboring areas, and less attention has been paid in the variations of them on monthly timescale. In this study, the structure, maintenance mechanism of the March Leading Eurasian Wave Train (LEWT), and its impact on the TP during 1980–2018 were investigated using reanalysis and meteorological observation data and a General Circulation Model (GCM). The positive interaction between synoptic-scale eddies and the mean flow in its upstream portion and the trapped effect of the climatological subtropical jet waveguide both play important roles in propagating and maintaining LEWT. During the positive phase of the LEWT, the barotropic energy conversion process over the southeastern TP can efficiently extract kinetic energy from climatological mean flow and further maintain the lower tropospheric southwesterly winds and northeasterly winds. As a result, the intensified (weakened) moisture transport, anomalous ascending (descending) motion and resultant above-normal (below-normal) precipitation appear on the western (southeastern) TP. Moreover, the anomalous warm high located over the southeastern TP causes pronounced surface air temperature warming through hydrostatic balance. GCM simulations further verify that the wave propagation from the North Atlantic and Western Europe to the southeastern TP can significantly influence the TP climate. The results would provide theoretical references for accurate climate prediction and aid the prevention of natural disasters over the TP.

1 Introduction

The Tibetan Plateau (TP) is characterized by complex terrain and a heterogeneous underlying surface (Qiu 2008; Han et al. 2021). Its huge elevated thermal forcing from spring to summer and dynamical blocking effectively regulate atmospheric circulation and associated moisture transport over the Eurasian continent, thereby controlling the summer monsoon onset and pattern of precipitation (Wu et al. 2007, 2012; Wang et al. 2008, 2014). In turn, the climate variability on the TP is influenced by mid-latitude and subtropical westerlies and the Asian monsoon system (Yu et al. 2011a; Zhou et al. 2019; Liu et al. 2020; Han et al. 2021; Gao et al. 2021). The TP is also known as the Asian water tower owing to many Asian rivers being located there (Xu et al. 2008). Precipitation is one of the most important factors in recharging the Asian water tower and generating latent heat, which can further modulate circulation and affect climate variability in the Asian Summer Monsoon region (Yu et al. 2011b; Hu and Duan 2015; He et al. 2019).

✉ Yimin Liu
lym@lasg.iap.ac.cn

1 Key Laboratory of Land Surface Process and Climate Change in Cold and Arid Regions, Northwest Institute of Eco-Environment and Resources, Chinese Academy of Sciences, Lanzhou, China

2 Nagqu Station of Plateau Climate and Environment, Northwest Institute of Eco-Environment and Resources, Chinese Academy of Sciences, Nagqu, Xizang, China

3 State Key Laboratory of Numerical Modeling for Atmospheric Sciences and Geophysical Fluid Dynamics (LASG), Institute of Atmospheric Physics, Chinese Academy of Sciences, Beijing, China

4 College of Earth and Planetary Sciences, University of Chinese Academy of Sciences, Beijing, China

5 Collaborative Innovation Center for Western Ecological Safety, Lanzhou University, Lanzhou, China

6 State Key Laboratory of Cryospheric Sciences, Northwest Institute of Eco-Environment and Resources, Chinese Academy of Sciences, Lanzhou, China

Published online: 31 October 2022

From a climatological perspective, boreal spring is the transitional season from winter to summer, with a decrease in the temperature meridional gradient, meridional migration of the jet stream, maintenance of wave activities, snow melting, and the appearance of persistent precipitation (Kuang and Zhang 2005; Wan and Wu 2007; Kuang et al. 2007; Zhang et al. 2017; Chen et al. 2020). Focusing on the TP, sensible heating becomes dominant in the TP heat source starting in March, and a significantly enhanced area is found over the inner and southeastern TP, where sensible heating exceeds 60.0 W/m^2 (Zhao et al. 2018). It is well known that sensible heating in these areas can trigger cyclonic circulation and even the onset of the South Asian Summer Monsoon, bringing abundant water vapor and precipitation to the TP and southeastern China through southwesterlies of both mechanically and thermally forced cyclonic circulation (Wan and Wu, 2007; Wu et al. 2012). In addition, water vapor flux transported by southwesterlies from the Bay of Bengal causes pre-monsoon precipitation from high altitudes of the Central Himalaya to the southeastern TP, which occurs beginning in March and can contribute 20–40% of the annual total precipitation (Ouyang et al. 2020). Moreover, heavy snowfall over the TP also predominantly occurs in spring (Zou and Cao, 1989; Liu et al. 2021), and it can cause snow-related disasters over the eastern and central TP, such as losses in animal husbandry (Gao and Qiu, 2011; Wei et al. 2017). Furthermore, spring snow depth anomalies on the TP can be associated with summer monsoonal precipitation in East Asia (Xiao and Duan 2016; Duan et al. 2018). Springtime surface air temperature in the TP may be a new precursor for sub-seasonal to seasonal climate prediction and is significantly linked to atmospheric circulation and associated snow anomalies that occur in February (Xue et al. 2018; Zhang et al. 2019). Therefore, clarifying the mechanism of climate variability over the TP in early spring can not only improve climate prediction on the TP and its neighboring areas to prevent natural disasters, but also advance our knowledge of the processes involved on the changing Asian water tower.

Atmospheric wave trains over the Eurasian continent play crucial roles in regional climate variability through anomalous horizontal thermal, moisture, and even vertical motions and aerosol transport along with the propagation of wave trains (Bueh and Nakamarua, 2007; Zhang et al. 2017; Chen et al. 2020; Li et al. 2020). Many efforts have also been devoted to the climate impact of Eurasian wave trains on the TP during different seasons on decadal and interannual scales. In boreal winter, wave trains from the Arctic and mid-high latitudes can propagate to the TP along the trapped subtropical jet waveguide, bringing dynamic and moist conditions favoring anomalous snowfall over the TP (Zhang et al. 2019; Liu et al. 2020). In spring, the unique decadal cooling shift during March and April in the southeastern TP can be attributed to eastward propagation from North Africa and the resulting positive cloud-temperature feedback during the positive phase of the North Atlantic oscillation (NAO) (Yu and Zhou 2004; Li et al. 2005, 2008). At the interannual scale, the quasi-steady Rossby wave trains triggered by the spring North Atlantic Sea surface temperature anomaly can maintain persistent snow cover starting in autumn and enhance westerly flow, resulting in sensible heating over the TP (Cui et al. 2015; Wang et al. 2019; Yu et al. 2021). The springtime quasi-steady Rossby wave train triggered by persistent diminished snowpack over Ural facilitates an enhanced subtropical westerly jet at the southern edge of the TP and ascending motion that combines with mesoscale updrafts to waft aerosols up and over the Himalayas onto the TP (Li et al. 2020). As the jet stream migrates to mid-latitude regions via seasonal thermal forcing over the TP, the summertime silk road pattern and wave trains triggered by North Atlantic Sea surface temperature anomalies extend to the TP along the mid-latitude jet, causing decadal wetting and warming shifts in the inner and northern TP through intensified moisture transport and anomalous warm highs (Zhou et al. 2019; Gao et al. 2021; Sun et al. 2020; Han et al. 2021). At the interannual scale, the positive phase of the NAO leads the anomalous anticyclone over the southern TP through eastward wave propagation, with weakening climatological moisture convergence and associated precipitation over that region (Wang et al. 2017).

The springtime climatological mean state changes rapidly, and pre-monsoon precipitation over the southeastern TP starts in March. Therefore, in this study, we defined March as early spring and focused on Eurasian atmospheric circulation and TP climate anomalies to explore the following questions. Does the favorable atmospheric wave train of the early spring climate anomaly occur over the TP on the interannual scale? What is the propagation and maintenance mechanism of the wave train? What is the linkage between wave train and climate anomalies over the TP? How can we reproduce this linkage in a General Circulation Model (GCM)? This study aims to understand the mechanisms of precipitation and surface air temperature anomalies in March over the TP by investigating the anomalous circulation and associated moisture transport processes during 1980–2018. The rest of this study is arranged as follows. Sect 2 describes the data, model, and methodology used in this study, including the simplified dry GCM. Sect 3 examines the March climatology mean circulation and explains the propagation and maintenance of the Eurasia wave train. Further, we explore the linkage between wave trains and climate anomalies over the TP and reproduce it in a GCM. Sect 4 presents a summary of this study.

2 Data, general circulation model and methods

2.1 Data

The Japanese 55 year reanalysis (JRA-55) dataset (Kobayashi et al. 2015) and ERA5 reanalysis data (Hersbach et al. 2020) are used in the present study. The data can be archived at the Earth's surface, pressure levels, and hybrid level. Surface variables contain surface air temperature and precipitation. Horizontal winds (U and V component), vertical velocity, geopotential height, temperature, and specific humidity in the isobaric surface are classified into pressure level variables. Vertical diffusion heating, convective heating, large-scale condensation heating, and temperature at hybrid level are also used in numerical tests. The horizontal resolutions for surface and pressure level data are 1.25°×1.25° and 0.25°×0.25° in JRA-55 and ERA5, respectively. For hybrid level data, the chosen resolution is 0.5625°×0.5625°. To verify the reanalysis data results, station meteorological observation data contain daily mean surface air temperature and precipitation provided by the China Meteorological Administration (CMA) and high resolution monthly mean land precipitation (0.25°×0.25°) derived from the Global Precipitation Climatology Centre dataset (Schneider et al. 2014) are included in this study.

2.2 General circulation model

The dry spectral dynamical core of the NCAR Community Atmosphere Model (CAM) version 5.4, with the idealized physical configuration based on Held and Suarez (1994), can act as an alternative to full physics parameterizations. The chosen horizontal resolution is spectral T85 truncation.

The radiative forcing parameterized as Newtonian relaxation of the temperature field to the zonal symmetric radiative equilibrium temperature T^r and external diabatic heating Q are imposed as follows in the temperature T prognostic equation:

$$\frac{\partial T}{\partial t} = \bullet\bullet\bullet + k_t(\phi,\sigma)(T - T^r(\phi,p)) + Q(\lambda,\phi,p), \quad (1)$$

where λ, ϕ, σ, p, t and k_t are the longitude, latitude, hybrid vertical coordinate, pressure, time, and radiative equilibrium temperature damping strength, respectively. The surface radiative equilibrium temperature (Schneider and Bordoni, 2008; Siu and Bowman, 2019) is described as follows:

$$T_s^r(\phi) = T^r_{equator} - \Delta_h(sin^2\phi - 2sin\phi_0 sin\phi). \quad (2)$$

The optical thickness of the atmosphere d_0 (Schneider, 2004) is expressed as follows:

$$d_0(\phi) = \left[\frac{T_s^r(\phi)}{T^r_{min}}\right]^4 - 1. \quad (3)$$

Then, the radiative equilibrium temperature T^r (Siu and Bowman, 2019) that depends on latitude and pressure is expressed as follows:

$$T^r(\phi,p) = T^r_{min}\left[1 + d_0(\phi)(\frac{p}{p_0})^\alpha\right]^{\frac{1}{4}} \quad (4)$$

In (2)–(4), $T^r_{equator}$, Δ_h, ϕ_0, p_0, and α are the equatorial temperature, temperature difference between pole and equator, latitude of maximum surface radiative equilibrium, reference surface pressure and scale-height ratio, respectively. The selected values are shown in Table 1, while the Rayleigh damping of momentum $\vec{V}$ is imposed to represent planetary boundary layer (extent is 0.85 in hybrid vertical coordinate) friction. It can be expressed as follows:

$$\frac{\partial \vec{V}}{\partial t} = \cdots + k_v(\sigma)\vec{V} \quad (5)$$

2.3 Methods

The horizontal wave-activity flux (W) can be used to describe the propagation of the atmospheric wave train because it is parallel to the local group velocity of the

Table 1 Selected parameters of the idealized physics package

Description	Symbol	Value
Equatorial temperature	$T^r_{equator}$	315 K
Pole-to-equator temperature difference	Δ_h	65 K
Latitude of maximum surface radiative equilibrium temperature	ϕ_0	0°N
Minimum radiative equilibrium temperature	T^r_{min}	200 K
Extent of the planetary boundary layer	σ_{PBL}	0.85
Radiative equilibrium temperature damping strength in the free atmosphere	k_a	1/40 day^{-1}
Radiative equilibrium temperature damping strength near the surface	k_s	1/4 day^{-1}
Scale-height ratio	α	3.5
Reference surface pressure	p_0	1000 hPa

stationary Rossby wave. It is calculated following Takaya and Nakamura (2001):

$$W = \frac{p}{2|\overline{V}|}\begin{cases}\overline{u}\left(\psi_x'^2 - \psi'\psi_{xx}'\right) + \overline{v}\left(\psi_x'\psi_y' - \psi'\psi_{xy}'\right) \\ \overline{u}\left(\psi_x'\psi_y' - \psi'\psi_{xy}'\right) + \overline{v}\left(\psi_y'^2 - \psi'\psi_{yy}'\right),\end{cases} \tag{6}$$

where $\overrightarrow{V}=(u,v)$ and ψ denote horizontal winds and the geostrophic stream function, respectively. The overbar and prime indicate climatological means for the 1980–2018 period and anomalies. Subscripts x and y represent the zonal and meridional derivations.

The synoptic-scale eddy-generated geopotential height tendency can be written as follows (Lau and Holopainen, 1984; Lau and Nath, 2014; Xu et al. 2019):

$$\left(\frac{\partial z}{\partial t}\right)_{eddy} = \frac{f}{g}\nabla^{-2}\left[\nabla \bullet \left(\overline{\overrightarrow{V'}\xi'}\right)\right] \tag{7}$$

Here, z, g, and f are the geopotential height, acceleration of gravity, and Coriolis parameter, respectively. ξ' and $\overrightarrow{V'}$ denote the synoptic-scale vorticity and horizontal winds that subject daily fields to a 2–8 days bandpass filter (Chen et al. 2020).

The atmospheric baroclinicity in this study is represented by the Eady growth rate, which is calculated according to the following relationship (Eady, 1949; Hoskins and Valdes, 1990):

$$\sigma_{BI} = 0.31\frac{f}{N}\frac{\partial u}{\partial z} \tag{8}$$

and N is the Brunt-Vaisala frequency.

Following previous studies (Kosaka and Nakamura 2006; Kosaka et al. 2009), the conversion of kinetic energy from the mean flow, denoted CK, can be written as follows:

$$CK = \frac{v'^2 - u'^2}{2}\left(\frac{\partial \overline{u}}{\partial x} - \frac{\partial \overline{v}}{\partial y}\right) - u'v'\left(\frac{\partial \overline{u}}{\partial y} + \frac{\partial \overline{v}}{\partial x}\right) \tag{9}$$

To extract the Leading Eurasian Wave Train (LEWT) in early spring and increase the reliability of the results, the Rotational EOF (REOF) analysis (Horel, 1981; Hannachi et al. 2007) was performed for the 250 hPa anomalous meridional wind in March based on JRA-55 and ERA5 after weighting by the cosine of latitude (North et al. 1982) over the 0°–150°E, 30°–90°N region. The above region is selected because it corresponds to the large standard deviation of meridional winds during spring, implying significant wave activities (Chen et al. 2020). The two datasets show a similar anomalous pattern of the first REOF mode, which accounts for 17.4% and 18.5% of the total variance in JRA-55 and ERA5, respectively. The above spatial pattern is characterized by a wave-like structure over Eurasian mid-high latitudes, with centers of anomalous southerlies over the Europe Plain and Eastern Siberia, and the center of the anomalous northerly are over Western Siberia (Fig. 1a, b). Therefore, we defined this mode as the LEWT. The principal component of REOF1 (RPC1) exhibits significant interannual and interdecadal variations. To quantify the LEWT's interannual variability and its climate impact, an index (named as LEWTI) was defined as the sum of area-averaged anomalous southerly wind with the domains (45°–75°N, 5°–35°E; 45°–75°N, 105°–135°E) minus anomalous northerly wind with the domain (40°–75°N, 55°–90°E). Furthermore, the RPC1 and LEWTI are subjected to a 2.5–4 years bandpass filter and normalized to account for the significant signal on interannual variation that is mainly focused on this interval. The correlation coefficient between them reaches as high as 0.92 (Fig. 1c), indicating that the LEWTI can provide a feasible representation of the spatiotemporal variations in the LEWT during 1980–2018.

3 Results

3.1 Climatological mean state

The observed climatological mean circulation, moisture transport, and precipitation in March are shown in Fig. 2. In the upper troposphere (250 hPa), the typical feature of the winter monsoon still remains over the Eurasian continent. Specifically, the broad trough extends from northeastern Asia to Japan, the weak trough is located over the European plain, and the high-pressure ridge controls the North Atlantic. For westerlies, the strong jet stream (Fig. 2b, contours) has a maximum south of Japan, North Africa and the Arabian Peninsula. The position of the jet core is consistent with the largest meridional temperature gradient at 700 hPa for thermal wind balance (Fig. 2a, shaded). In addition, the jet stream strongly affects the weather and climate locally as well as in the downstream regions by means of modulating the activity of transient eddies along itself and acting as a waveguide to facilitate zonal propagation of Rossby waves (Yang et al. 2002; Ren et al. 2008). The maximum value of the stationary wavenumber (Fig. 2b, shaded) is well matched with the distribution of the subtropical jet, further indicating the trapped effect along the subtropical jet (Hoskins and Karoly, 1981). The water vapor transported into the TP by the subtropical jets in terms of climatology mainly occurs through the southeastern and western edges (Fig. 2c, d), and its convergence can be observed in the abovementioned two regions and south of China. The precipitation over land areas of the Eurasian continent mainly occurs on the southeastern and western edges of the TP, South China, with the amount exceeding 60 mm (Fig. 2e). Additionally, the large values of precipitation variance also located at abovementioned

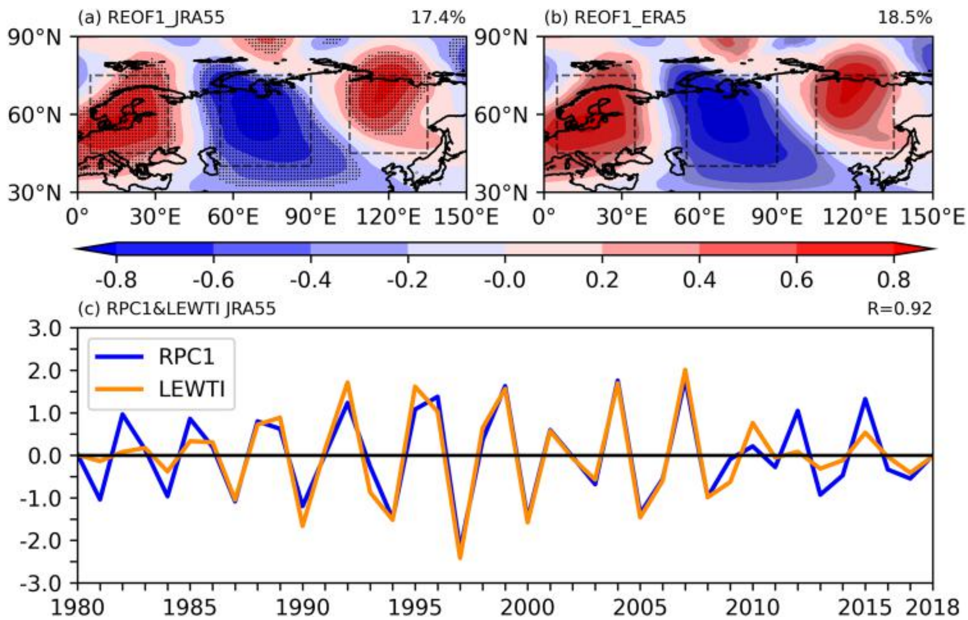

Fig. 1 The correlation coefficients between March mean meridional winds at 250 hPa with its REOF 1 over the region (30°–90°N, 0°–150°E) derived from **a** JRA-55 and (**b**) ERA5 with their variance contributions at the top right of each panel. The dots denote values exceeding the 95% confidence level. **c** Filtered and normalized time series of the first principal component (RPC1; blue line) of meridional wind derived from JRA-55. The yellow line in **c** shows the LEWTI defined as the filtered and normalized sum of meridional winds among the rectangles with positive values (45°–75°N, 5°–35°E) and (45°–75°N, 105°–135°E) and negative values (40°–75°N, 55° –90°E) multiplied by − 1 shown in **a**. The R in **c** is the correlation coefficient between the two indices

regions (Fig. 2f), implying the strong variability over these regions. Some biases among different datasets are also noticed. When compared to the patterns of moisture transport derived from JRA-55 and ERA5, moisture convergence occurs south of the Indio-China peninsula from JRA-55; however, divergence occurs from ERA5.

3.2 Structure and dynamics of the March LEWT

Based on the JRA-55 and ERA5 datasets, the anomalous circulation over the Eurasian continent associated with the LEWT index is shown in Fig. 3. The spatial pattern of 250 hPa regressed zonal wind indicates that westerlies over the North Atlantic at approximately 60°N, Eastern Europe, Western Siberia, the Bay of Bengal, and the Indio-China peninsula have weakened. Accelerated westerlies appear over the Atlantic at approximately 40°N, North Africa, the TP and North China (Figs. 3a, b). Patterns of LEWT are demonstrated in Fig. 3c, d, which present the anomalous 250 hPa eddy geopotential height (difference of geopotential height from its zonal mean) and wave fluxes. Over the North Atlantic and Europe plain, a significant anomalous cyclonic pattern appears in situ during March. Moreover, the wave train is markedly reinforced over this region, splitting into two branches. One branch propagates to higher latitudes, and the other branch propagates southeastward to the southeastern TP. Overall, the LEWT of cyclonic and anticyclonic anomalies located over the European plain and West Siberia causes weakened westerlies over mid-higher latitudes, and cyclonic and anticyclonic anomalies appear on Baikal Lake and southeastern TP, thereby accelerating the jet over the TP and North China. The spatial patterns derived from JRA-55 resemble those from ERA5. The mechanism of the above patterns will be explained in the next section.

Previous studies indicate that the atmosphere over mid-high latitudes has strong internal variability and baroclinicity, in which synoptic-scale transient eddies transport heat and momentum flux to redistribute the heat and momentum space, accompanied by jet streams (Fang and Yang, 2016; Jiang et al. 2017; Xu et al. 2019; Liu et al. 2020). Therefore, the feedback forcing from transient eddies plays a crucial role in the maintenance of low-frequency flow anomalies. Figure 4a, b show regression maps of the anomalous Eady growth rate at 700 hPa and geopotential height tendency induced by the transient eddies at 250 hPa onto the LEWTI. The increased (decreased) lower tropospheric baroclinicity simultaneously appears on north of the TP (North Atlantic to West Siberia), which coincides with the anomalous westerlies pattern (Fig. 3a) for the increased baroclinicity favors more transient eddies and accelerates the eddy-driven jet via eddy feedback forcing to low-frequency flow, and vice versa (Fang and Yang, 2016; Jiang et al. 2017). Figure 4b illustrates that the anomalous cyclonic and anticyclonic transient eddy forcing emerge to the south and north of the

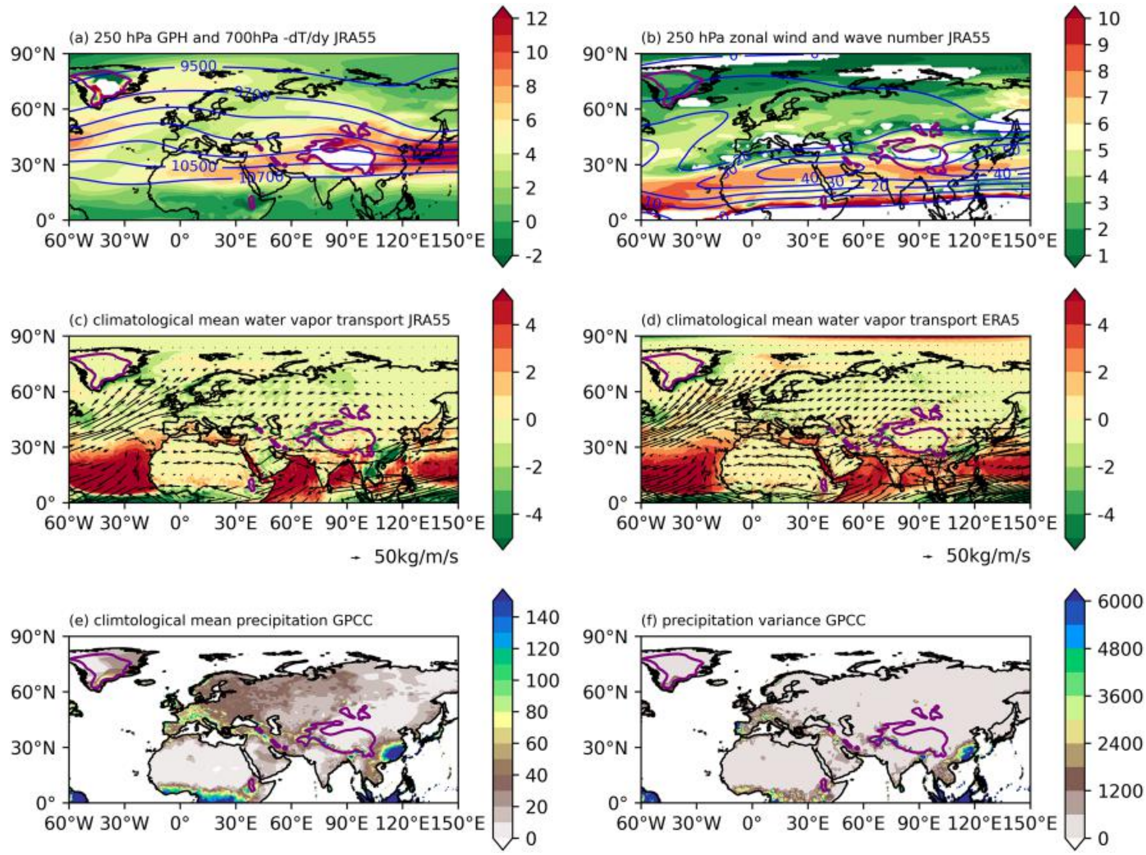

Fig. 2 The mean March 250-hPa geopotential heights (contours; unit: gpm) and 700-hPa temperature meridional gradient (shaded; unit: 10^{-6} K/m) **a**, 250-hPa zonal wind (contour; unit: m/s) and stationary wavenumber (shaded) **b**, vertically integrated water vapor transport (vector; unit: kg/m/s) and its convergence (shaded; unit:10^{-5} kg/m^2/s) derived from JRA-55 **c** and ERA5 **d**. **e** The mean March accumulated precipitation (unit: mm) and its variance derived from GPCC (unit: mm^2). The purple line indicates the 2000 m elevation contour

westerly deceleration over mid-high latitudes. Moreover, an anticyclonic transient eddy forcing appears on the TP, coincide with increased lower tropospheric baroclinicity north of the TP (Fig. 4a). The patterns of transient eddy forcing are identical in phase with the centers of the LEWT, especially on anomalous low centers over the European plain, Baikal Lake, and anomalous high centers over West Siberia and the southeastern TP. The above results suggest that the transient eddy feedback forcing can maintain the wave pattern in the upper troposphere.

As mentioned above, the LEWT can become reinforced and split into two branches over the European plain. Further explanation can be given through determination of the regressed Eady growth rate, transient eddy forcing, zonal wind, and eddy geopotential height latitude-altitude section averaged between 30°W-10°E. Figure 4c shows that lower-level atmospheric baroclinicity decreased north of 50°N and increased south of 50°N. Westerly anomalies show the equivalent barotropic deceleration (acceleration) north (south) of 50°N (Fig. 4e) for the feedback forcing from transient eddies to mean flow. Furthermore, the equivalent barotropic transient eddy cyclonic forcing and eddy geopotential height anomalies appear south of the deceleration of atmospheric baroclinicity and zonal wind. Therefore, they are in phase with each other in the latitudinal direction, which can maintain and reinforce the LEWT. Additionally, climatological subtropical jet during March acts as a wave guide, which can trap the south branch wave train within it.

3.3 The impact of the March LEWT on the Tibetan Plateau

In this section, the climate impact of the March LEWT on Eurasia continent, especially on the TP, will be examined through the analysis of patterns of anomalous three-dimensional circulation and temperature at 500 hPa, water vapor transport, and precipitation associated with the March LEWT. Figure 5a displays the anomalous eddy geopotential heights and horizontal flows at 500 hPa. While, the amplitude of the eddy geopotential heights at 500 hPa is obviously less than that at 250 hPa. By combining the pattern of temperature anomalies (Fig. 5c), there

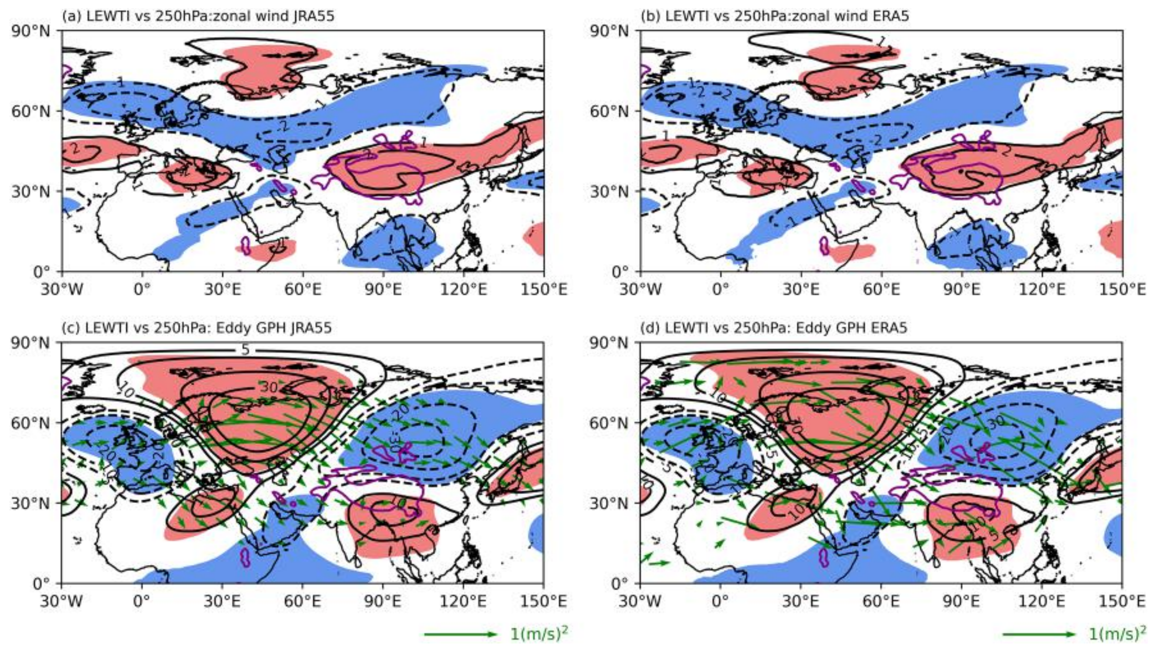

Fig. 3 The March mean 250-hPa zonal wind (contour; unit: m/s; CI = 1 m/s) regressed onto LEWTI derived from JRA-55 **a** and ERA5 **b**. The March mean 250-hPa eddy geopotential height (contour; unit: gpm; CI = ±5, 10, 20, 30 gpm) anomalies and associated horizontal component of the wave-activity flux (green vector; unit: m^2/s^2) regressed onto the LEWTI derived from JRA-55 (**c**) and ERA5 (**d**). The light shading indicates the 95% confidence level. The purple line indicates the 2000 m elevation contour

exists an anomalous warm high over the southeastern TP. Meanwhile, Southerly (northerly) wind anomalies appear on the western (southeastern) TP. According to the simplified vertical velocity equation and Sverdrup balance (Wu and Liu, 2000; Wu et al., 2015; Yu et al. 2021), anomalous southerly winds can lead to horizontal convergence and ascending motion, and conversely, anomalous ascending and descending motions appear on the western and southeastern TP (Fig. 5b).

The maintenance of the above patterns is important to the precipitation and surface temperature anomalies over the TP. The mechanism can be explained by estimating the local barotropic energy conversion (*CK*) at 500 hPa associated with LEWT, and the evaluation is based on the conversion of kinetic energy from the climatological mean flow. In the mid-low troposphere, the negative meridional shear of climatological zonal wind ($\frac{\partial \bar{u}}{\partial y} < 0$) can be seen along the south flank of the TP. Positive *CK* is concentrated over the southwestern TP, where the exit of the subtropical westerly jet ($\frac{\partial \bar{u}}{\partial x} < 0$) is located and the southwestern wind anomalies ($-u'v' < 0, v'^2 > u'^2$) are observed between the cyclonic and anticyclonic anomalies. However, a negative *CK* is shown over the southeastern TP, where the entrance of the East Asian westerly jet ($\frac{\partial \bar{u}}{\partial x} > 0$) is located and the northwestern wind anomalies ($-u'v' > 0, v'^2 > u'^2$) are shown (Fig. 5d).

To examine the vertical distribution of temperature and vertical velocity anomalies associated with the LEWT, the latitude-altitude section of temperature averaged between 90°E and 100°E and the longitude-altitude section of vertical velocity averaged from 27°N to 32°N are shown in Fig. 5e and Fig. 5f, respectively. The results show that the anomalous warm center over the southern TP (with the warmest anomaly near 500 hPa) and anomalous cold over the mid-latitude strengthen the meridional temperature gradient. The vertical velocity anomalies can extend to 200 hPa and show a dipole pattern over the TP, with anomalous ascending (descending) motions over the western (southeastern) TP.

To further diagnose the spatial pattern of precipitation over the TP associated with the LEWT during March, the patterns of vertically integrated water vapor transport and its divergence anomalies derived from the JRA-55 and ERA5 datasets are examined in Fig. 6a, b. The results show that water vapor convergence over the southeastern (western) TP decreased (strengthened), compared to the climatological mean pattern (Fig. 2c, d). It results from the strengthened moisture imports from the Arabian Sea and weakened moisture imports from north of the Bay of Bengal. The pattern of anomalous water vapor transport is similar to that of anomalous atmospheric circulations at 500 hPa, with anomalous anticyclonic circulations located over the southeastern TP. Moreover, strengthened moisture transport is also observed from southern China to Japan. Overall, the favorable conditions of anomalous circulations modulate water vapor transport, causing the dipole pattern

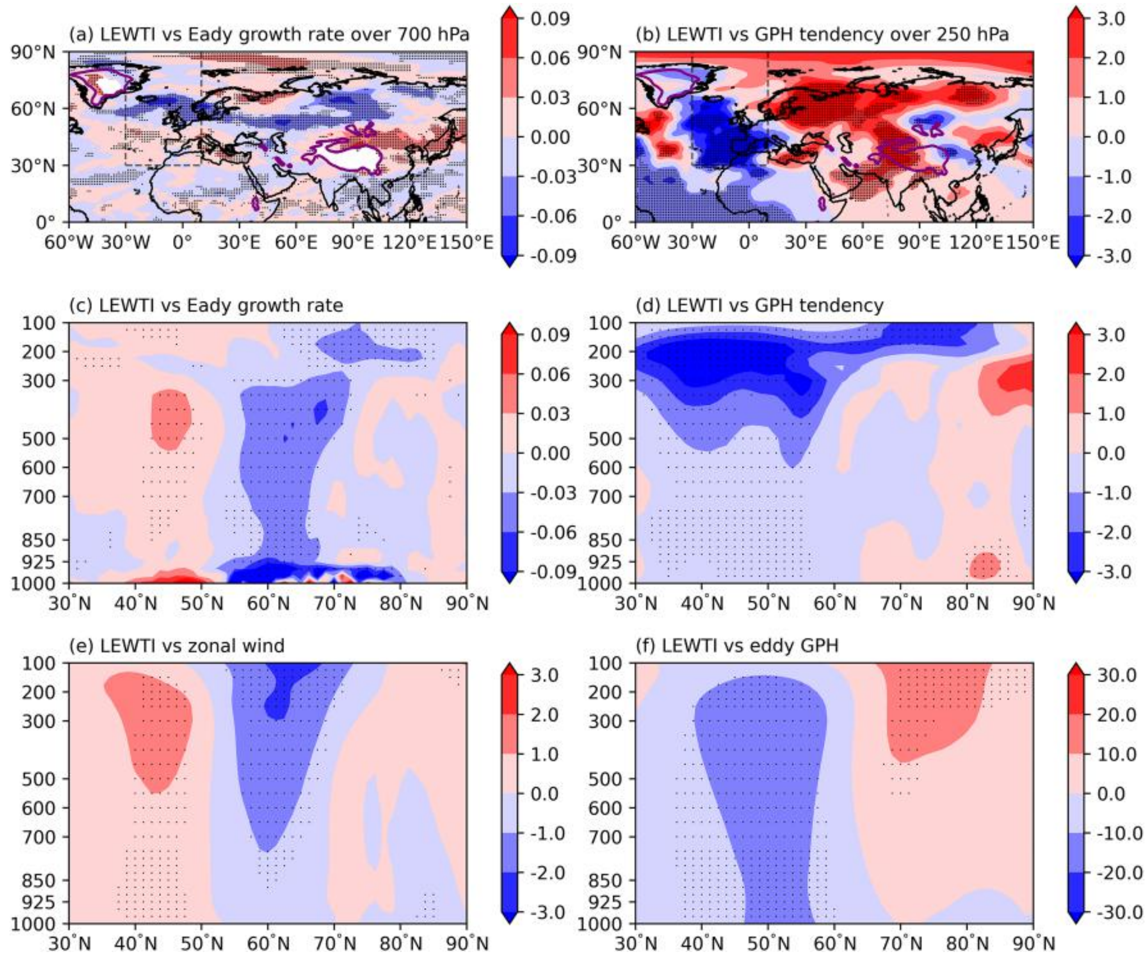

Fig. 4 **a** The March mean 700-Pa Eady growth rate (unit:1/day) and **b** 250-hPa geopotential height tendency induced by transient eddies (unit: gpm/day) anomalies regressed onto LEWTI derived from JRA-55. **c** The latitude-height cross section of Eady growth rate (unit: 1/day), **d** geopotential height tendency induced by transient eddies (unit: gpm/day), **e** zonal wind (unit: m/s) and **f** eddy geopotential height (unit: gpm) anomalies averaged from 30°W to 10°E onto the LEWTI derived from JRA-55. The dots denote values exceeding the 95% confidence level. The purple line indicates the 2000 m elevation contour. The rectangles (30°–90°N, 30°W–10°E) in (**a**) and (**b**) are domains for average and analysis in (**c**)–(**f**)

of precipitation in the TP and enhancing precipitation in South China during March (Fig. 7). Notably, although the patterns of anomalous precipitation are similar among the JRA-55, ERA5, and GPCC datasets, the difference still exists, with the enhanced precipitation derived from ERA5 and GPCC appearing downstream of the Brahmaputra River (Fig. 7b, c), which may originate from the difference in the horizontal resolution of the three datasets because JRA-55 has a resolution of 1.25°×1.25°, while the others have a resolution of 0.25°×0.25°. The above bias among the three datasets suggests that the variability of precipitation and its mechanism under complex terrain and heterogeneous land space is still a challenging question. To further evaluate the LEWT impact on TP precipitation during early spring, we select two regions where large variance of precipitation (Fig. 2f) and significant regressed values (Fig. 7c) occur based on GPCC. Specifically, one region locates in southern and inner TP, confining in 82.125°E-95.125°E, 22.125°N-35.125°N and within negative regressed precipitation onto LEWTI, while, another locates in western TP, confining in 70.125°E-80.125°E, 30.125°N-40.125°N and within positive regressed precipitation. Explained variance of time series constructed by area mean precipitation over the western TP minus that over the southern and inner TP regressed onto LEWT is 14.5%, passing the 95% significant level. Above result further reveal that LEWT can have a significant impact on dipole pattern of TP early spring precipitation.

The composite analysis results are used to compare the positive phase of the LEWT with the negative phase of the LEWT, examine the regressed results (Fig. 8) and explore the surface air temperature anomalies over the TP (Fig. 9). The criterion of sample year selection is listed as follows: LEWTI values exceeding 0.5 are positive phase years, while

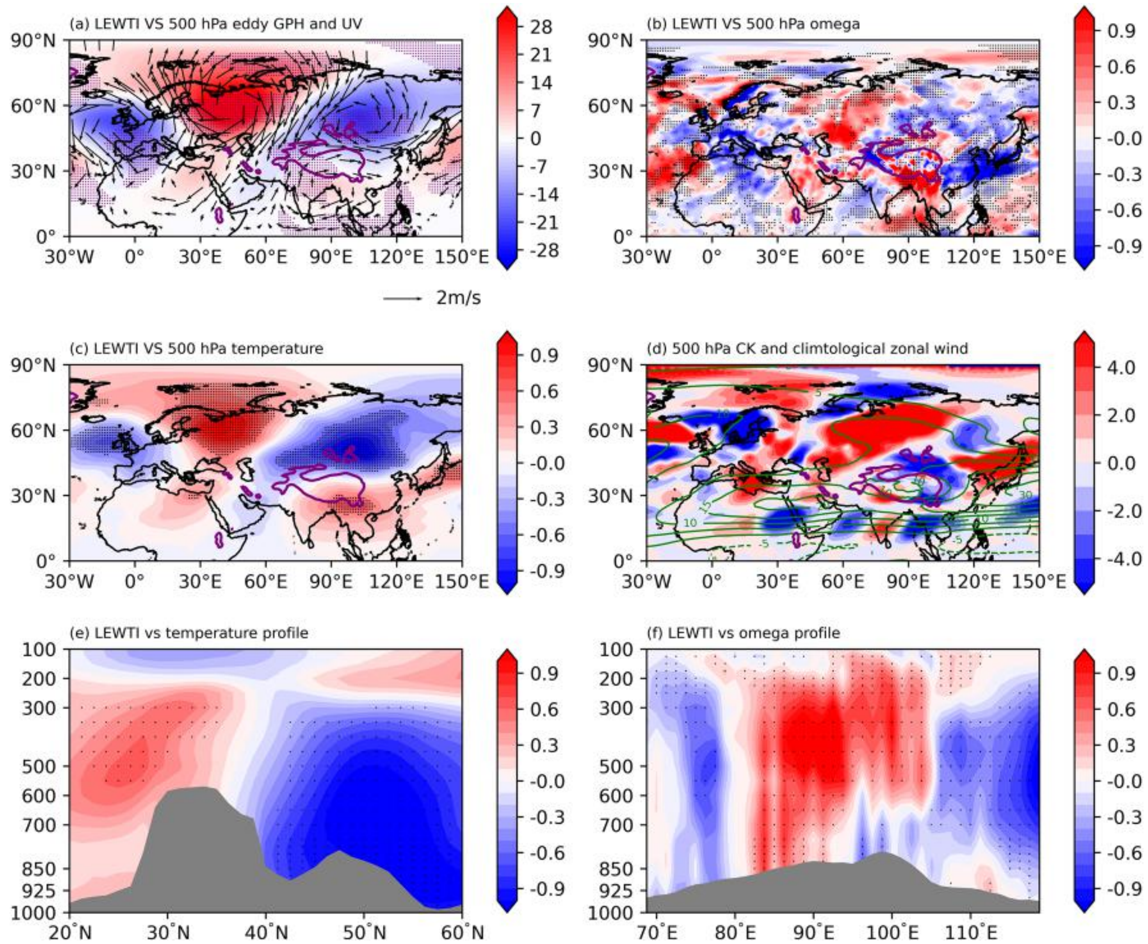

Fig. 5 **a** The March mean eddy geopotential height (shaded; unit: gpm) and winds (vector; unit: m/s), **b** vertical velocity (unit: 0.01 Pa/s), **c** temperature(unit: K) at 500 hPa regressed on LEWTI. **d** The climatological mean 500-hPa zonal wind (green contour. unit: m/s; CI = 5 m/s) and kinetic energy conversion between anomalous circulations and climatology mean flows (unit: 10^{-6} m^2s^{-3}). **e** The latitude-height cross section of temperature anomalies (unit: K) averaged from 90°E to 100°E, and **f** the longitude-height cross section of vertical velocity anomalies (unit: 0.01pa/s) averaged from 27°N to 32°N regressed onto the LEWTI. The above results are derived from JRA-55. The dots and vectors denote values exceeding the 95% confidence level. The purple line indicates the 2000 m elevation contour

LWETI values below − 0.5 are negative phase years. The selected anomalous years are shown in Table 2.

There are significant positive geopotential height anomalies over the southeastern TP, with negative geopotential height anomalies over mid-latitudes of the Eurasian continent (Fig. 8a). The patterns are consistent with those in the regressed results (Fig. 3c, d). Due to descending motion at 500 hPa over the southeastern TP (Fig. 8b), precipitation over the TP is weakened (Fig. 8c–d). However, ascending motion at 500 hPa appears on the western TP and southeastern China (Fig. 8b), thereby leading to above-normal precipitation, which can be observed from GPCC and station observational data (Fig. 8c–d). Meanwhile, surface air temperature over the southeastern TP (Fig. 8e) is warmed by the anomalous warm high center via the hydrostatic balance (Li et al. 2022), and it also can be displayed in the site observational data (Fig. 8f).

3.4 Numerical simulations

3.4.1 Climatological means

In this study, the GCM runs with prescribed topography (Fig. 9, blue contour) and imposed diabatic heating after deviating from its zonal mean, interpolating into a model grid, then, it is spatially smoothed following Sardeshmukh and Hoskins's method (Fig. 9, shaded) (Sardeshmukh and Hoskins, 1984). Additionally, during March, the climatological mean vertical diffusion heating due to surface sensible heating is mainly concentrated in the TP, Indian Peninsula,

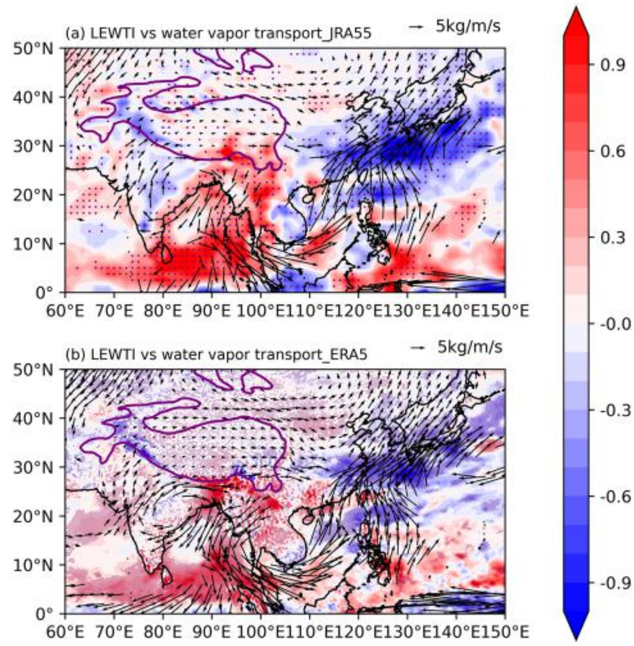

Fig. 6 **a** The March mean vertically integrated moisture transport (vector; unit: kg/m/s) and its divergence (shaded; unit: 10^{-5} kg/m^2/s) anomalies regressed onto the LEWTI derived from JRA-55. **b** As in (a), but derived from ERA5. Purple dots and vectors denote values exceeding the 95% confidence level. The purple line indicates the 2000 m elevation contour

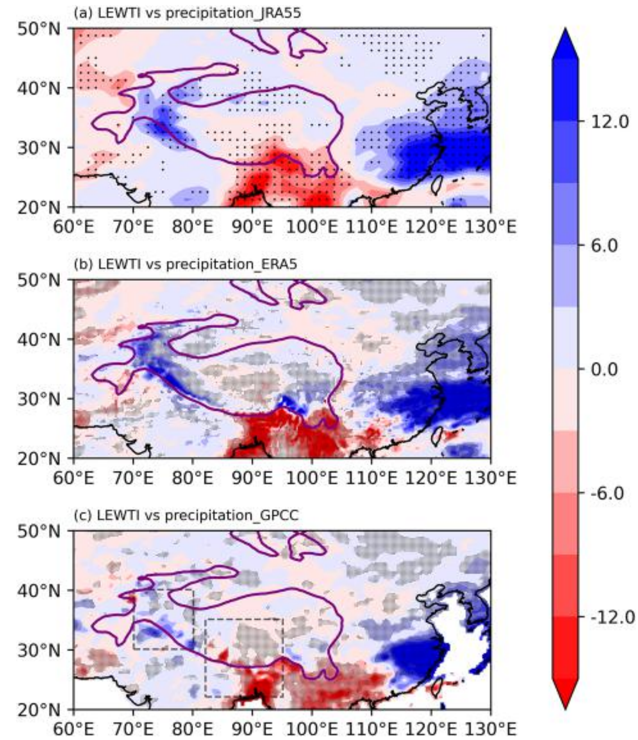

Fig. 7 The March accumulated precipitation (unit: mm) anomalies regressed onto the LEWTI. The results are derived from **a** JRA-55, **b** ERA5, and **c** GPCC. The dots denote values exceeding the 95% confidence level. The purple line indicates the 2000 m elevation contour. The rectangles with positive values (30.125°–40.125°N, 70.125°–80.125°E) and positive values (22.125°–35.125°N, 82.125°–95.125°E) are shown in (c)

and Eastern Africa, while convective and condensation heating is located in the southern Hemisphere between 0°S and 30°S. Thus, vertical diffusion heating is imposed on the continent, and convective and condensation heating is imposed on the tropical region. We performed a set of control experiments with the GCM to derive different initial fields. The model is perpetually running in March for 5 years, and the 2 year results are spun off; next, 50 initial conditions that deviated from the last 3 years' mean temperature are used for the ensemble simulation. Then, the climatology and sensitivity experiments, each with 50 members, are integrated throughout March.

The GCM can reproduce the main feature of the climatological mean tropospheric circulation in the Northern Hemisphere during March (Fig. 10). In mid-high latitudes, the upper tropospheric broad trough over northeastern Asia, a weak trough over the European plain, and a ridge over the North Atlantic can be reproduced (Fig. 10a). The patterns of the subtropical jet stream and East Asian jet stream are also consistent with the reanalysis results (Fig. 10a, Fig. 2a). However, some biases should be noted when compared to the observational results (Fig. 2). GCM underestimates the Northern Hemisphere geopotential height to some extent (Fig. 10a). The strength of the subtropical jet and East Asian jet is also weakened in the GCM (Fig. 10a), which can be attributed to the negative bias of the meridional temperature gradient at a lower level (Fig. 10b, Fig. 2a) under thermal wind balance. The climatological mean temperature and vertical velocity in the lower level are also displayed through their spatial pattern at 26th hybrid-level (30th hybrid-level is labeled as the lowest level) (Fig. 10c, d), which is approximately equivalent to pressure levels of 500 ~ 450 hPa over the TP. The temperature also remains the wintertime feature, in which cold air mainly controls the continent and warm air is located in the tropics and ocean (Fig. 10c). The ascending motion over the southeastern and western TP and South China favors persistent rainfall in these regions. The descending motion generally controls the tropical region. In mid-high latitudes, the ascending and descending motions appear alternately, while, their magnitudes are obviously weaker than those in subtropical and tropical regions (Fig. 10 d).

3.4.2 Simulations for the March LEWT

In the sensitivity experiment, to quality mimic the LEWT, three-dimensional March mean temperature anomalies

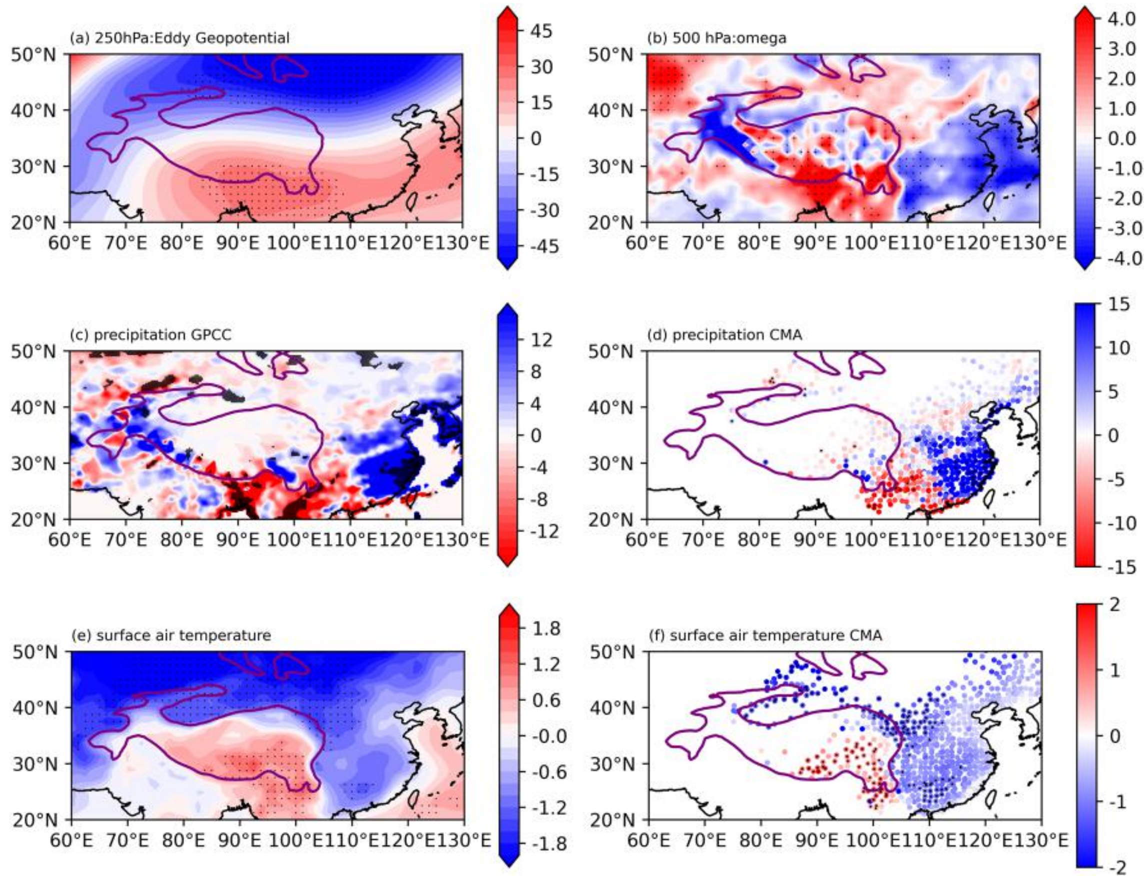

Fig. 8 **a** The composite maps of LEWT differences between positive and negative phases in 500-hPa eddy geopotential height (unit: gpm), **b** vertical velocity (unit:0.01 Pa/s), **c** precipitation derived from GPCC (unit: mm) and (**d**) CMA station observational data (unit: mm), **e** surface air temperature anomalies derived from JRA-55 (unit: K) and (**f**) CMA station observational data (unit: K). The dots denote values exceeding the 90% confidence level. The purple line indicates the 2000 m elevation contour

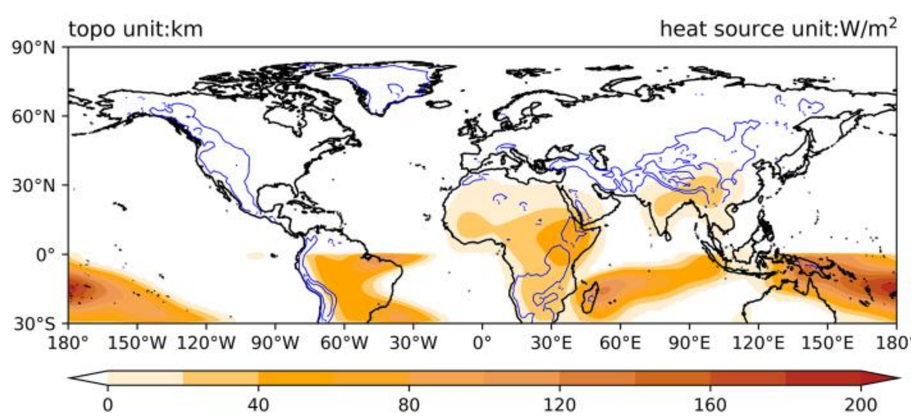

Fig. 9 The topography (blue contour, unit: km) and diabatic heating (shaded, unit: W/m^2) in the General Circulation Model

Table 2 Years with positive and negative phases of the March LEWT

Years of positive phase	Years of negative phase
1988, 1989, 1992, 1995, 1996, 1998, 1999, 2001, 2004, 2007	1987, 1990, 1993, 1994, 1997, 2000, 2003, 2005, 2006, 2008, 2009

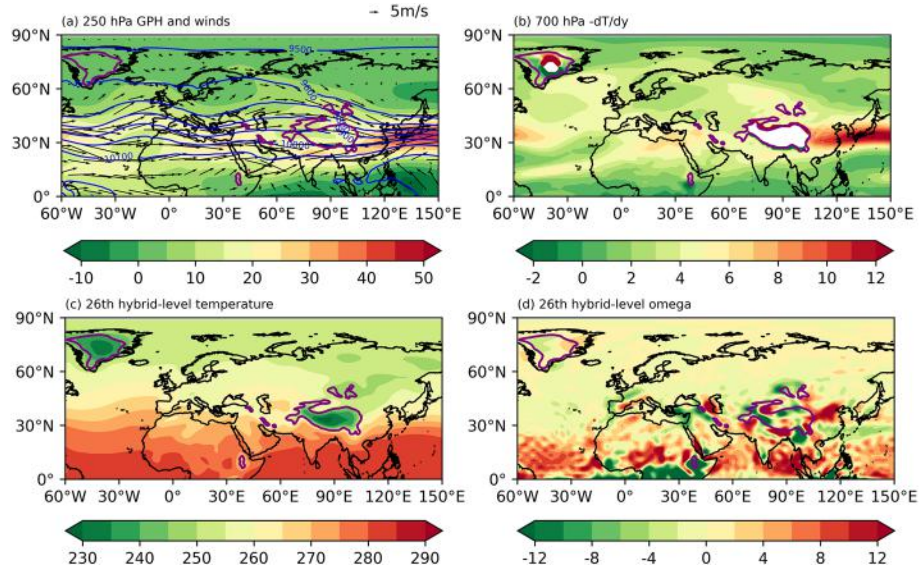

Fig. 10 **a** The GCM simulations of climatological March mean 250-hPa geopotential height (blue contour; unit: gpm; CI = 100 gpm), zonal wind (shaded; unit: m/s), horizontal winds (vector; unit: m/s) and **b** 700-hPa temperature meridional gradient (unit:10^{-6} K/m). **c** The simulated climatological March mean temperature (unit: K) and **d** vertical velocity (unit:0.01 Pa/s) at 26th hybrid-level (30th hybrid-level is labeled as the lowest level). The purple line indicates the 2000 m elevation contour

(positive cases minus negative cases) from the North Atlantic to Western Europe (Fig. 11) are considered the anomalous heat sink and are imposed on the external diabatic heating term for Eq. (1) during the entire integration period.

The simulated LEWT and its associated anomalies in temperature and vertical velocity can be obtained through the ensemble difference between the sensitivity and climatology tests. Fifty member ensembles are conducted to reduce the uncertainties from the initial conditions and internal variations in the GCM. The 250-hPa and 500-hPa dynamical responses of the anomalous cold center over the North Atlantic and Western Europe (Fig. 12 a, b) resemble the spatial pattern of the LEWT that has a barotropic structure and contains the anomalous anticyclone over the southeastern TP (Fig. 2c, d, and Fig. 5a). According to the hydrostatic balance, warm (cold) responses at 26th hybrid-level coincide with the anticyclonic (cyclonic) centers in the simulated LEWT, except for anomalous anticyclone over Caspian Sea (Fig. 12c). Moreover, the anomalous descending (ascending) motions over the southeastern (western) TP that favor anomalous precipitation over the TP are also reproduced at 26th hybrid-level. To further explore how long the anomalous anticyclone can appear over the southeastern TP, we calculated the 5 day running averaged area mean vorticity at 8th hybrid-level within the domain (24.5°– 31.5°N, 87.2°– 92.8°E) in the climatology and sensitivity tests. After 10 days of integration, the obviously negative bias between the two experiments appears and tends to be steady, except for little difference between day-20 to day-22 (Fig. 13). This finding further

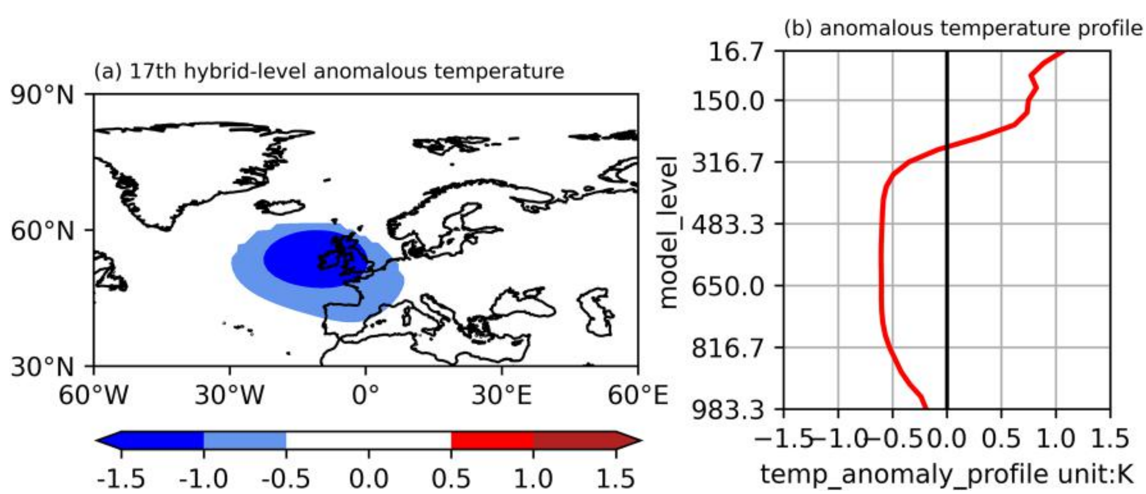

Fig. 11 **a** The 17th hybrid-level (30th hybrid-level is labeled as the lowest level) temperature anomalies (unit: K), and (**b**) area mean within the domain (39.9°-62.3°N,15.5°W-15.5°E) temperature anomalies profile along hybrid-level

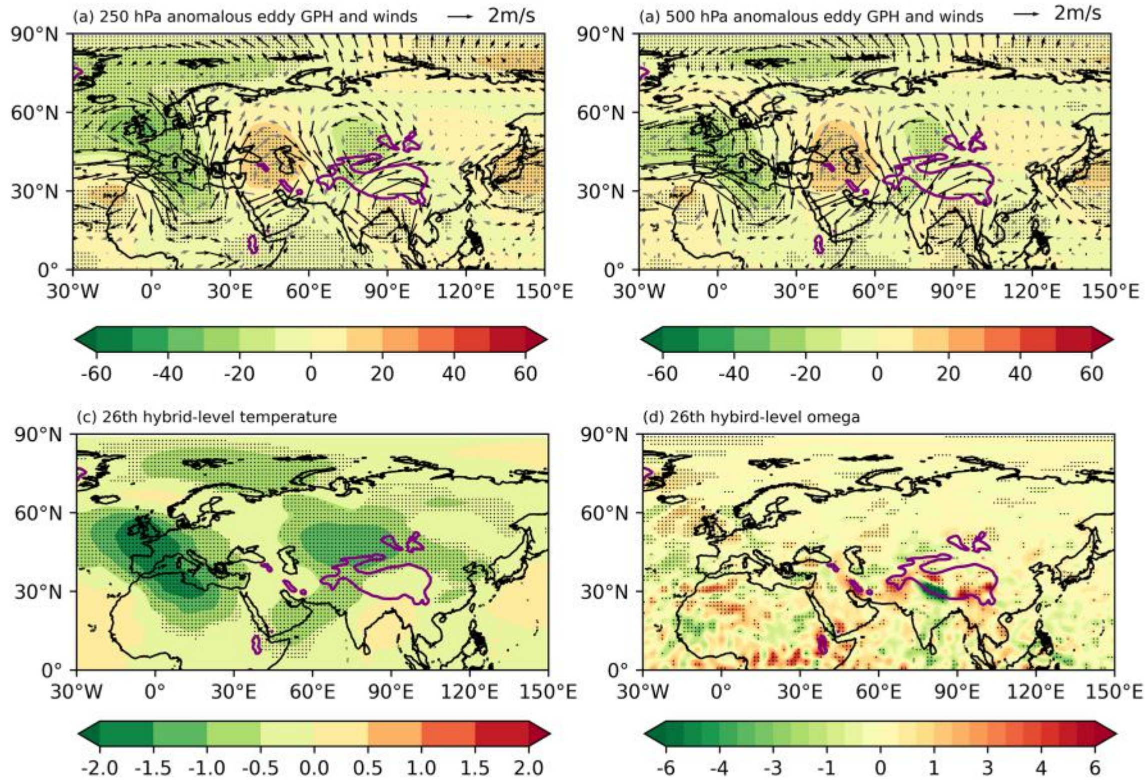

Fig. 12 **a** The GCM simulations of eddy geopotential height (shaded; unit: gpm) and wind anomalies at 250 hPa (vector; unit: m/s). **b** As in **a**, but at 500 hPa. **c** The GCM simulations of temperature (unit: K) and vertical velocity (unit: 0.01 Pa/s) anomalies at 26th hybrid level (30th hybrid-level is labeled as the lowest level). The dots and black vectors denote values exceeding the 90% confidence level. The purple line indicates the 2000 m elevation contour

indicates that the perturbed North Atlantic and Europe plain thermal conditions can propagate to the TP within one month in March.

4 Conclusions and discussion

The relationship between the March Leading Eurasian Wave Train (LEWT) and climate anomalies over the TP and associated mechanisms were investigated through thermodynamic and dynamic determination of reanalysis and observational data and numerical sensitivity tests in the GCM. The results indicate that the leading REOF mode of meridional wind on the interannual scale can be characterized as a wave train that splits into two branches. Thus, the propagation and maintenance mechanisms of this wave train are explored for wave-activity flux, subtropical jet waveguide, and feedback forcing between transient eddies and mean flow. The anomalous cold low center over the North Atlantic and Western Europe act as a Rossby wave

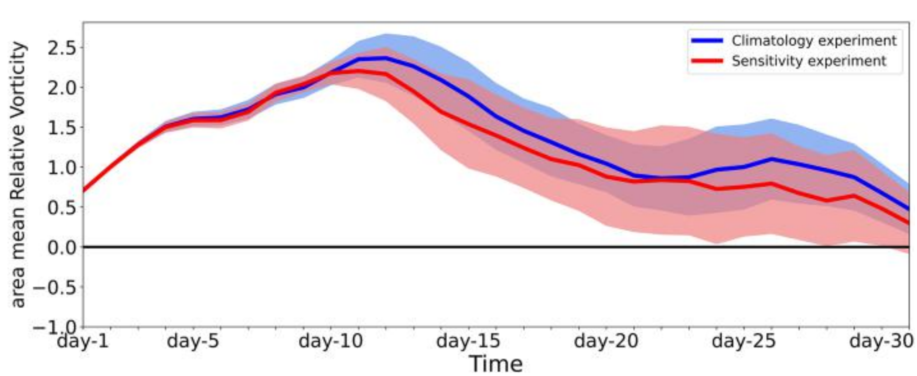

Fig. 13 The time series of the area mean relative vorticity (unit:10^{-5} s^{-1}) at 8th hybrid-level (30th hybrid-level is labeled as the lowest level) over the southern TP. Shading areas indicate one standard deviation for 50 members in climatology and sensitivity tests

source for positive feedback forcing from anomalous synoptic eddy activities. The downstream portion of the wave train extending over the Eurasian continent can propagate to Baikal Lake and the southern TP under modest feedback forcing from transient eddies and the trapped effect of the waveguide along the subtropical jet.

The remote influence on the TP via propagation of the south branch wave train and kinetic energy along the subtropical jet is apparent. The pattern of precipitation anomalies, with the positive center located over the western TP and a negative center located over the southeastern TP, can be explained by anomalous winds over the southeastern TP. The anomalous southwesterly (northeasterly) winds can be maintained through effective kinetic energy conversion over the western (southeastern) TP, where the exit of the subtropical jet and entrance of the East Asian jet are located. The resultant increased moisture transport and enhanced ascending motion appear on the western TP, whereas the opposite signal appears on the southeastern TP. For surface air temperature, reanalysis data and site observational data both show significant anomalous warm patterns in the southeastern TP, which is caused by the anomalous warm high located over the southeastern TP through hydrostatic balance.

The model results demonstrate that the GCM can reproduce the March LEWT. Corresponding to the imposed anomalous cooling temperature from the North Atlantic to Western Europe in the GCM, the anomalous warm high and anticyclonic circulation over the southeastern TP and anomalous ascending (descending) motion over the western (southeastern) TP are primarily simulated. These simulated dynamic and thermodynamic processes favor the dipole pattern of TP precipitation, in which above-normal (below-normal) precipitation appears on the western (southeastern) TP.

The connection between LEWT and TP climate during early spring has been examined using both observations and numerical model simulations in the present study. However, other oceanic forcing factors, such as ENSO and sea surface temperature anomalies in Indian Ocean and North Atlantic (Cui et al. 2015; Jin et al. 2016; Zhao et al. 2018; Yu et al. 2021) also can act as important drivers on the variations of TP climate during springtime. Therefore, further study on the synergistic impacts of anomalous mid-high latitudes forcing in sub-seasonal timescale and tropical oceanic forcing in interannual and even decadal timescale on TP climate variation in different timescale is necessary.

On the other hand, the simulated anomalous lower tropospheric temperature over the TP and ascending motion over southern China (Fig. 12 c, d) are weaker comparing to the composite results (Fig. 8 b, e, f). During springtime, changes of land surface thermal conditions caused by snow decrement and freeze–thaw of seasonally frozen ground (Zhang et al. 2017; Luo et al. 2020) will influence atmospheric circulation over Eurasia. In future study, sensitivity experiments using climate model with full physics will reduce the bias and better reproduce the interaction between the changes of TP thermal condition and atmospheric circulation.

Acknowledgements We thank three anonymous reviewers for their constructive comments and helpful suggestions, which helped us to improve our paper. The authors are grateful for the availability of GCM from the website of https://www.cesm.ucar.edu/models.

Author contributions All the authors made contributions to the conceptualization of this work. Yaoxian Yang did analyses and drafted the work, others revised the manuscript.

Funding This research was supported jointly by National Natural Science Foundation of China (Grants 91937302, 91837208, 42075043 and 42122034), the Second Tibetan Plateau Scientific Expedition and Research Program (2019QZKK0103), the Strategic Research Program of the Chinese Academy of Sciences (Grant NO. XDA2006010101) and the Youth Innovation Promotion Association CAS.

Data availability The ERA5 data are available from https://cds.climate.copernicus.eu. The JRA-55 data are available from https://rda.ucar.edu. The GPCC data are available from https://climatedataguide.ucar.edu/climate-data/gpcc-global-precipitation-climatology-centre. The meteorological observation data provided by the China Meteorological Administration (CMA) are available from http://www.nmic.cn.

Declarations

Conflict of interests There are no competing interests.

Code availability The codes used in this study are available from authors on reasonable request.

References

Bueh C, Nakamura H (2007) Scandinavian pattern and its climatic impact. Q J R Meteorol Soc 133:2117–2131

Chen S, Wu R, Chen W et al (2020) Structure and dynamics of a springtime atmospheric wave train over the North Atlantic and Eurasia. Clim Dyn 54(11–12):5111–5126

Cui Y, Duan A, Liu Y et al (2015) Interannual variability of the spring atmospheric heat source over the Tibetan Plateau forced by the North Atlantic SSTA. Clim Dyn 45:1617–1634

Duan A, Xiao Z, Wang Z (2018) Impacts of the Tibetan Plateau winter/spring snow depth and surface heat source on Asian summer monsoon: a review. Chin J Atmo Sci 42(4):755–766 (**in Chinese**)

Eady E (1949) Long waves and cyclone waves. Tellus 1:33–52

Fang J, Yang X (2016) Structure and dynamics of decadal anomalies in the wintertime midlatitude North Pacific ocean-atmosphere system. Clim Dyn 47:1989–2007

Gao M, Qiu J (2011) Characteristics and distribution law of major natural disasters in Tibetan Plateau. J Arid Land Resour Environ 08:101–106 ((**in Chinese**))

Gao K, Duan A, Chen D (2021) Interdecadal summer warming of the Tibetan Plateau potentially regulated by a sea surface temperature anomaly in the Labrador Sea. Int J Climatol 41(S1):2633–2643

Han Y, Ma W, Yang Y et al (2021) Impacts of the Silk Road pattern on the interdecadal variations of the atmospheric heat source over the Tibetan Plateau. Atmos Res 2:105696

Hannachi A, JolliffeI T, Stephenson DB (2007) Empirical orthogonal functions and related techniques in atmospheric science: a review. Int J Climatol 27:1119–1128

He C, Wang Z, Zhou T et al (2019) Enhanced latent heating over the Tibetan Plateau as a key to the enhanced East Asian summer monsoon circulation under a warming climate. J Clim 32:3373–3388

Held I, Suarez M (1994) A proposal for the intercomparison of the dynamical cores of atmospheric general circulation models. Bull Am Meteor Soc 75:1825–1830

Hersbach H, Bell B, Berrisford P et al (2020) The ERA5 global reanalysis. Q J R Meteorol Soc 146:1999–2049

Horel J (1981) A rotated principal component analysis of the interannual variability of the Northern Hemisphere 500mb height field. Mon Weather Rev 109:2080–2092

Hoskins B, Karoly D (1981) The steady linear response of a spherical atmosphere to thermal and orographic forcing. J Atmos Sci 38:1179–1196

Hoskins B, Valdes P (1990) On the existence of storm-tracks. J Atmos Sci 47(15):1854–1864

Hu J, Duan A (2015) Relative contributions of the Tibetan Plateau thermal forcing and the Indian ocean sea surface temperature basin mode to the interannual variability of the east Asian summer monsoon. Clim Dyn 45:2697–2711

Jiang Y, Yang X, Liu X et al (2017) Anthropogenic aerosol effects on East Asian winter monsoon: the role of black carbon-induced Tibetan Plateau warming. J Geophys Res Atmos 122:5883–5902

Jin R, Qi L, He J (2016) Effect of oceans to spring surface sensible heat flux over Tibetan Plateau and its influence to East China precipitation. Acta Oceanol Sin 38:83–95 ((**in Chinese**))

Kobayashi S, Yukinari O, Yayoi H et al (2015) The JRA-55 reanalysis: general specifications and basic characteristics. J Meteorol Soc Jpn 93:5–48

Kosaka Y, Nakamura H (2006) Structure and dynamics of the summertime Pacifc-Japan teleconnection pattern. Q J R Meteorol Soc 132:2009–2030

Kosaka Y, Nakamura H, Watanabe M et al (2009) Analysis on the dynamics of a wave-like teleconnection pattern along the summertime Asian jet based on a reanalysis dataset and climate model simulations. J Meteorol Soc Jpn 87:561–580

Kuang X, Zhang Y (2005) Seasonal variation of the East Asian subtropical westerly Jet and Its association with heating fields over East Asia. Adv Atmos Sci 22(6):831–840

Kuang X, Zhang Y, Liu J (2007) Seasonal Variations of the East Asian subtropical westerly Jet and its thermal mechanism. Acta Meteor Sin 21(2):192–203

Lau N, Holopainen E (1984) Transient eddy forcing of the time-mean flow as identified by geopotential tendencies. J Atmos Sci 41:313–328

Lau N, Nath M (2014) Model simulation and projection of European heat waves in present-day and future climates. J Clim 27:3713–3730

Li J, Yu R, Zhou T et al (2005) Why is there an early spring cooling shift downstream of the Tibetan Plateau? J Clim 18(22):4660–4668

Li J, Yu R, Zhou T (2008) Teleconnection between NAO and climate downstream of the Tibetan Plateau. J Clim 21(18):4680–4690

Li F, Wan X, Wang H et al (2020) Arctic sea-ice loss intensifies aerosol transport to the Tibetan Plateau. Nat Clim Change 10:1037–1044

Li J, Xie T, Tang X et al (2022) Influence of the NAO in wintertime surface air temperature over the east Asia: multidecadal variability and decadal prediction. Adv Atmos Sci 39(4):625–642

Liu X, Liu Y, Wang X et al (2020) Large-scale dynamics and moisture sources of the precipitation over the western Tibetan Plateau in boreal winter. J Geophys Res Atmos 125(9):2019032133

Liu L, Ma Y, Yao N et al (2021) Diagnostic analysis of a regional heavy snowfall event over the Tibetan Plateau using NCEP reanalysis data and WRF. Clim Dyn 56(7):2451–2467

Luo S, Wang J, Pomeroy J et al (2020) Freeze-thaw changes of seasonally frozen ground on the Tibetan Plateau from 1960 to 2014. J Clim 33(21):1–57

North G, Moeng F, Bell T et al (1982) The latitude dependence of the variance of zonally averaged quantities. Mon Weather Rev 110:319–326

Ouyang L, Yang K, Lu H et al (2020) Ground based observations reveal unique valley precipitation patterns in the central Himalaya. J Geophys Res Atmos 125(5):e2019JD031502

Qiu J (2008) China: the third pole. Nature News 454:393–396

Ren X, Zhang Y, Yang X (2008) Connections between wintertime jet stream variability, oceanic surface heating, and transient eddy activity in the north Pacific. J Geophys Res Atmos 113:D21119

Sardeshmukh P, Hoskins B (1984) Spatial smoothing on the sphere. Mon Weather Rev 112(12):2424–2529

Schneider T (2004) The tropopause and the thermal stratification in the extratropics of a dry atmosphere. J Atmos Sci 61:1317–1340

Schneider T, Bordoni S (2008) Eddy-mediated regime transitions in the seasonal cycle of a Hadley circulation and implications for monsoon dynamics. J Atmos Sci 65:915–934

Schneider U, Becker A, Finger P et al (2014) GPCC's new land surface precipitation climatology based on quality-controlled in situ data and its role in quantifying the global water cycle. Theor Appl Climatol 115(1):15–40

Siu L, Bowman K (2019) Forcing of the upper-tropospheric monsoon anticyclones. J Atmos Sci 76(7):1937–1954

Sun J, Yang K, Wang Y et al (2020) Why has the Inner Tibetan Plateau become wetter since 1990s? J Clim 33(19):8507–8522

Takaya K, Nakamura H (2001) A formulation of a phase-independent wave-activity flux for stationary and migratory quasi geostrophic eddies on a zonally varying basic flow. J Atmos Sci 58:608–627

Wan R, Wu G (2007) Mechanism of the spring persistent rains over southeastern China. Sci China Earth Sci 50:130–144

Wang B, Bao Q, Hoskins B et al (2008) Tibetan plateau warming and precipitation changes in east Asia. Geophys Res Lett 35:L14702

Wang Z, Duan A, Wu G (2014) Time-lagged impact of spring sensible heat over the Tibetan Plateau on the summer rainfall anomaly in East China: case studies using the WRF model. Clim Dyn 42:2885–2898

Wang Z, Duan A, Yang S et al (2017) Atmospheric moisture budget and its regulation on the variability of summer precipitation over the Tibetan Plateau. J Geophys Res Atmos 122:614–630

Wang Z, WuZhao RP et al (2019) Formation of snow cover anomalies over the Tibetan Plateau in cold seasons. J Geophys Res Atmos 124(9):4873–4890

Wei Y, Wang S, Fang Y et al (2017) Integrated assessment on the vulnerability of animal husbandry to snow disasters under climate change in the Qinghai-Tibetan Plateau. Glob Planet Change 157:139–152

Wu G, Liu Y (2000) Thermal adaptation, overshooting, dispersion, and surbtropical high. part I: thermal adaptation and overshooting. Chin J Atmos Sci 24:433–446 ((**in Chinese**))

Wu G, Liu Y, Wang T et al (2007) The influence of mechanical and thermal forcing by the Tibetan Plateau on Asian climate. J Hydrometeorol 8(4):770–789

Wu G, Liu Y, He B et al (2012) Thermal controls on the Asian summer monsoon. Sci Rep 2:404

Wu G, Duan A, Liu Y et al (2015) Tibetan Plateau climate dynamics: recent research progress and outlook. Natl Sci Rev 2(1):100–116

Xiao Z, Duan A (2016) Impacts of Tibetan Plateau snow cover on the interannual variability of the East Asian summer monsoon. J Clim 29(23):8495–8514

Xu X, Lu C, Shi X et al (2008) World water tower: an atmospheric perspective. Geophys Res Lett 35(20):L20815

Xu P, Wang L, Chen W (2019) The British-Baikal Corridor: a teleconnection pattern along the summertime polar front jet over Eurasia. J Clim 32:877–896

Xue Y, Diallo I, Li W et al (2018) Spring land surface and subsurface temperature anomalies and subsequent downstream late spring-summer droughts/floods in north America and East Asia. J Geophys Res Atmos 123:5001–5019

Yang S, Lau K, Kim K (2002) Variations of the East Asian jet stream and Asian–Pacific–American winter climate anomalies. J Clim 15(3):306–325

Yu R, Zhou T (2004) Impacts of winter-NAO on March cooling trends over subtropical Eurasia continent in the recent half century. Geophys Res Lett 31:L12204

Yu J, Liu Y, Wu G (2011a) An analysis of the diabatic heating characteristic of atmosphere over the Tibetan Plateau in winter II: Interannual variation. Acta Meteor Sin 58(5):513–522 ((**in Chinese**))

Yu J, Liu Y, Wu G (2011b) An analysis of the diabatic heating characteristic of atmosphere over the Tibetan Plateau in winter I: climatology. Acta Meteor Sin 69(1):89–98 ((**in Chinese**))

Yu W, Liu Y, Yang X et al (2021) Impact of North Atlantic SST and Tibetan Plateau forcing on seasonal transition of springtime South Asian monsoon circulation. Clim Dyn 56:559–579

Zhang R, Zhang R, Zuo Z (2017) Impact of Eurasian spring snow decrement on east asian summer precipitation. J Clim 30(9):3421–3437

Zhang Y, Zou T, Xue Y (2019) An Arctic-Tibetan connection on subseasonal to seasonal time scale. Geophys Res Lett 46:2790–2799

Zhao Y, Duan A, Wu G (2018) Interannual variability of late-spring circulation and diabatic heating over the Tibetan Plateau associated with Indian ocean forcing. Adv Atmos Sci 35(8):927–941

Zhou C, Zhao P, Chen J (2019) The interdecadal change of summer water vapor over the Tibetan Plateau and associated mechanisms. J Clim 32(13):4103–4119

Zou J, Cao C (1989) Climatological analysis of snowfall over the Qinghai-Xizang Plateau. Chin J Atmos Sci 13:400–409 ((**in Chinese**))